Available online at www.sciencedirect.com
SCIENCE DIRECT®
Journal of Magnetic Resonance 175 (2005) 177–184
JMR Journal of Magnetic Resonance
www.elsevier.com/locate/jmr

# Systematic approach to cutoff frequency selection in continuous-wave electron paramagnetic resonance imaging

Hiroshi Hirata [a,*], Toshiharu Itoh [a], Kouichi Hosokawa [a], Yuanmu Deng [b], Hitoshi Susaki [a]

[a] Department of Electrical Engineering, Yamagata University, Yonezawa, Yamagata 992-8510, Japan
[b] Center for Biomedical EPR Spectroscopy and Imaging, Davis Heart and Lung Research Institute, Ohio State University, Columbus, OH 43210, USA

Received 4 March 2005; revised 6 April 2005
Available online 10 May 2005

**Abstract**

This article describes a systematic method for determining the cutoff frequency of the low-pass window function that is used for deconvolution in two-dimensional continuous-wave electron paramagnetic resonance (EPR) imaging. An evaluation function for the criterion used to select the cutoff frequency is proposed, and is the product of the effective width of the point spread function for a localized point signal and the noise amplitude of a resultant EPR image. The present method was applied to EPR imaging for a phantom, and the result of cutoff frequency selection was compared with that based on a previously reported method for the same projection data set. The evaluation function has a global minimum point that gives the appropriate cutoff frequency. Images with reasonably good resolution and noise suppression can be obtained from projections with an automatically selected cutoff frequency based on the present method.
© 2005 Elsevier Inc. All rights reserved.

*Keywords:* EPR imaging; Deconvolution; Window function; Image reconstruction; Resolution

## 1. Introduction

Electron paramagnetic resonance (EPR) imaging can be used to visualize the distribution of unpaired electrons in a subject [1–5]. This is a noninvasive method for detecting free radicals in a living system. There have been impressive advances in EPR imaging techniques since the late 1980s [6–11], since free radicals play very important roles in biomedical studies. Since an electron spin system has an extremely short relaxation time compared to that of a nuclear spin system, most EPR imaging uses a continuous-wave (CW) detection protocol. While time-domain EPR spectroscopy and imaging at frequencies below 1 GHz are available for animal experiments at some laboratories [12–14], EPR imaging still requires CW-EPR instruments for paramagnetic materials with broader EPR absorption spectra.

Two methods are used to reconstruct EPR images from spectra with gradient magnetic fields, called projections. The most commonly used method is filtered back-projection (FBP) [15]. Furthermore, the direct Fourier transform reconstruction (DFTR) method is applicable not only to MRI [15–17] but also to EPR imaging [18,19]. In EPR imaging, the projection $f(x)$ with a magnetic field gradient is given by convolution of the spatial profile of unpaired electrons $g(x)$ and the line-shape function $h(x)$:

$$f(x) = \int_{-\infty}^{+\infty} g(x-\tau)h(\tau)\mathrm{d}\tau. \quad (1)$$

EPR imaging is a spectroscopic method for obtaining the function $g$ in Eq. (1), and deconvolution for each projection with a zero-gradient projection is performed to obtain the profile of unpaired electrons in the subject [20].

* Corresponding author. Fax: +81 238 26 3299.
*E-mail address:* hhirata@yz.yamagata-u.ac.jp (H. Hirata).

1090-7807/$ - see front matter © 2005 Elsevier Inc. All rights reserved.
doi:10.1016/j.jmr.2005.04.007

In the DFTR method, deconvolution of the measured projections with a zero-gradient projection is applied in the spatial frequency domain called $k$-space. A low-pass window function, e.g., the Hamming window function, is usually used to avoid the division-by-zero problem in $k$-space. In proton MRI, free-induction decay (FID) or spin echo signals are directly measured in the time domain as data in $k$-space. Therefore, there is no process of deconvolution in MRI. However, deconvolution is needed for EPR spectra with hyperfine coupling to obtain the spatial distribution of unpaired electrons.

Selection of the cutoff frequency in the low-pass window function is important for achieving good spatial resolution and noise suppression in the resultant EPR images. Since the spatial resolution is given by the effective width of the point spread function (PSF) [21], the relation between the PSF and the cutoff frequency of the window function should be taken into account when the bandwidth of the window function is determined. In practice, the cutoff frequency of the function is selected by trial and error through visual inspection [22]. If a systematic method was available for determining the appropriate cutoff frequency of the low-pass window function for deconvolution, it could significantly improve the reproducibility of EPR imaging and the ease of operation of an image reconstruction program. To eliminate the need for visual inspection and trial and error, a systematic approach to this problem is needed in EPR imaging techniques.

There have been several studies on how to automatically select the cutoff frequency. Sotgiu and co-workers [20] reported a method for selecting the cutoff frequency in the process of deconvolution in the spatial frequency domain. Their method determines the cutoff frequency from the level of noise in the power spectrum of the measured first-derivative EPR absorption spectrum. While this approach is reasonable in one-dimensional imaging, there are some technical difficulties in multi-dimensional EPR imaging. Each projection has different signal-to-noise ratios in general, and this leads to variation of the cutoff frequencies of the low-pass window function. If the cutoff frequency of the window function is changed in each projection, the resultant image is distorted. Recently, Deng et al. [23] proposed a statistical method for determining the appropriate cutoff frequency in EPR imaging. However, the relation between the cutoff frequency and the physical significance of the measurements was not investigated in their method.

This article describes a method for systematically determining the cutoff frequency for deconvolution in two-dimensional (2D) EPR imaging. The hypothesis is that the product of the effective width of the PSF and the noise level in the resultant image can be used as the evaluation function for cutoff frequency selection. This study was designed to demonstrate the concept of automatic cutoff frequency selection and to compare our results with those of a previously reported method using the same sample.

## 2. Methods

### 2.1. Requirements for spatial resolution and noise suppression

Cutoff frequency selection of the low-pass window function affects the image resolution and the signal-to-noise ratio (SNR) of the resultant EPR image, and is usually determined by trial and error through visual inspection. A practical problem in deconvolution of measured EPR spectra with a zero-gradient projection is how to select the appropriate spatial cutoff frequency for the window function being applied. A low-pass window function can avoid the division-by-zero problem in the high-frequency band during deconvolution. In addition to the resolution and noise of resultant EPR images, ease of operation is an important consideration for the further development of EPR imaging techniques in biomedical applications. This practical demand requires a systematic approach to cutoff frequency selection for the window function being applied.

For discrete-variable functions, the deconvolution of two functions, the projection $F(k)$ and the zero-gradient projection $H(k)$ in $k$-space, is given by

$$g(n) = \mathrm{IFT}\left\{\frac{F(k)}{H(k)}W(k)\right\}, \tag{2}$$

where IFT means the inverse Fourier transform, and $W(k)$ is the low-pass window function. The present problem is how to determine the cutoff frequency of function $W(k)$ to optimize the spatial resolution and the SNR in the resultant EPR image.

There are two criteria for image quality, i.e., the spatial resolution and the SNR. The resolution has to be as high as possible. To achieve this goal, the spectral information in the high-frequency band is essential. Thus, this requires a low-pass window function with a higher cutoff frequency. In contrast to the spatial resolution, the noise levels of the resultant images should be as low as possible. This requires a low-pass window function with a lower cutoff frequency to avoid errors in the high-frequency band that are caused by noise in the measured EPR spectra. The errors are amplified by small values in function $H(k)$ in Eq. (2), called the division-by-zero problem. These factors require contradictory settings of the low-pass window function, and consequently compromises are needed regarding the criteria that affect the resultant images.

### 2.2. Strategy of optimization

The strategy for automatic cutoff frequency selection is to use an evaluation function that gives a degree of

optimization for the two criteria mentioned above. We used the product of the effective width, i.e., the full width at half maximum (FWHM), and the noise level in the marginal area as the evaluation function. The effective width of the PSF of the localized point signal is used to estimate the spatial resolution. For the noise level of a resultant image, we used the maximum amplitude of the noise in the marginal area that ideally has no signals around the area of interest (AOI). At the global minimum point of the product, the cutoff frequency provides a strike job in the contradictory requirements in the resultant image. Fig. 1 illustrates the concept of the present strategy and the evaluation function. This can provide a useful criterion for automatic selection of the cutoff frequency in deconvolution in the DFTR method. This allows us to achieve stable image reconstruction without visual inspection.

### 2.3. Point spread function

The spatial resolution is presented by the effective width of the PSF, which can show the image profile of the localized point signal like a $\delta$-function. If the bandwidth in the spatial frequency domain is limited, the spatial distribution of the localized point signal has a broader profile in the resultant image. In discrete data processing, the FWHM of the PSF is defined by the effective width of the band-limited Kronecker delta function. The computation process in Fig. 1A takes place to give the FWHM of the PSF as a function of the cutoff frequency.

Using fast Fourier transform (FFT), the spectrum data in $k$-space is obtained from the localized point signal, i.e., the Kronecker delta function:

$$\delta[n] = \begin{cases} 1 & n = 1, \\ 0 & \text{otherwise.} \end{cases} \tag{3}$$

The discrete-variable function of the PSF is calculated as the band-limited Kronecker delta function:

$$\mathrm{PSF}[n] = \mathrm{IFT}\{\mathrm{FFT}\delta[n] \times W[k]\}. \tag{4}$$

We used the Hamming window function with the desired bandwidth in $k$-space $W_\mathrm{k}$ for function $W(k)$ in Eq. (4), and it is defined by

$$W[k] = \begin{cases} 0.54 + 0.46\cos\{\frac{\pi k}{W_k}\} & \frac{k}{W_k} < 1, \\ 0 & \text{otherwise.} \end{cases} \tag{5}$$

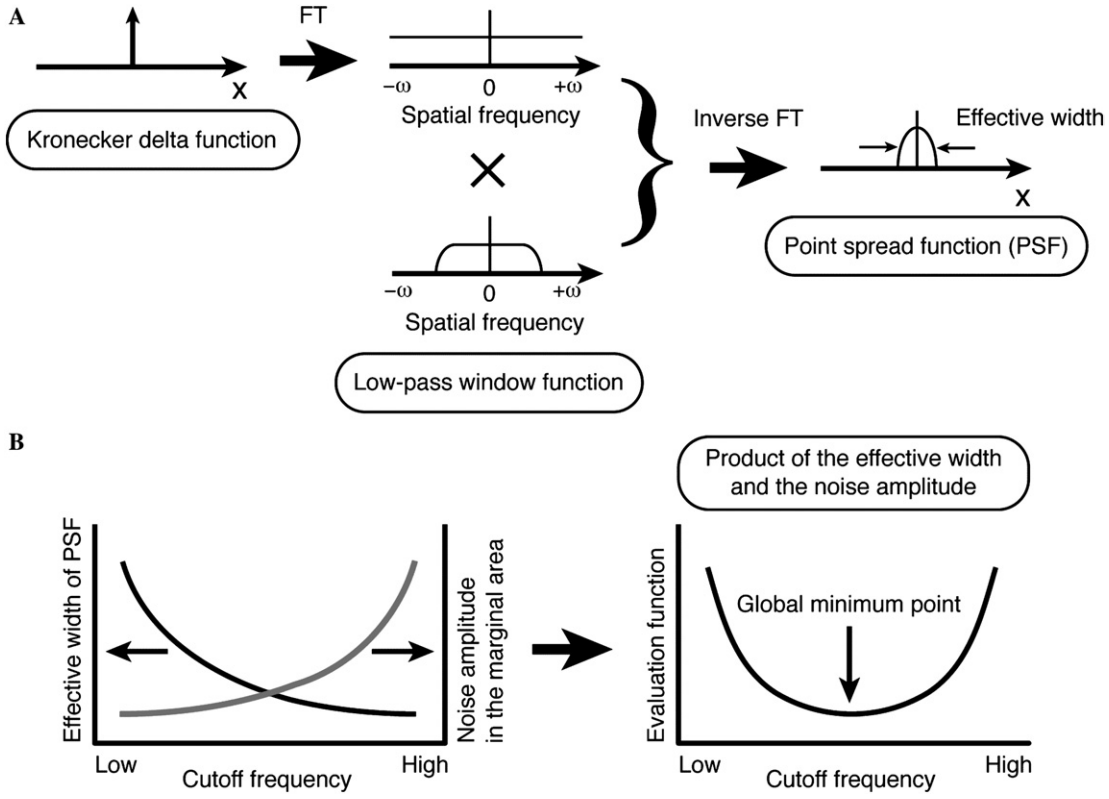


Fig. 1. Concept of optimizing the image resolution and noise suppression in CW-EPR imaging. (A) Effective width (full width at half maximum (FWHM)) of the point spread function (PSF) is calculated from the low-pass window function and the Kronecker delta function. The effective width shows the spatial resolution in resultant images. (B) Evaluation function for determining the cutoff frequency of the low-pass window function. Noise and artifacts are desired to be as low as possible. The product of the effective width of the PSF and the noise amplitude in the marginal area can be used as an evaluation function to optimize the cutoff frequency of a filter function used in deconvolution.

Finally, the FWHM of the PSF is obtained from the discrete data of the PSF. Linear interpolation between the data points is used to precisely determine the effective width.

### 2.4. Noise level estimation

To predict the noise level, we have to distinguish the signals due to EPR from noise in the resultant image. To make this possible, the noise level is considered in the marginal area of the AOI, as shown in Fig. 2. Here, we assumed that noise in the marginal area is similar to that in the AOI. We can always consider the signals at the outside of the resonator as noise or artifacts. The field of view (FOV) in a CW-EPR protocol with magnetic field gradients $\Delta B$ is given by

$$\mathrm{FOV} = \frac{B_{\mathrm{scan}}}{\Delta B}, \tag{6}$$

where $B_{\mathrm{scan}}$ is the width of magnetic field scanning. The magnetic field gradients and magnetic field scanning are chosen for experimental models such as the line width, the line-shape of the subject chemical species, and the AOI.

If the FOV is greater than the dimensions of the resonator, the resultant image has a marginal area that is around the AOI. We can search for the maximum amplitude of noise in the marginal area. Alternatively, it is possible to use the standard deviation $\sigma$ of the noise, and to multiply it by a factor to give the threshold for noise suppression. For example, the threshold that corresponds to $2\sigma$ gives the probability that the noise in the AOI beyond the threshold level is 2.3%. If the FOV and the dimensions of the resonator are comparable, the marginal area can not be used to measure the noise level. In such a case, a technique of zero-filled FT reconstruction can be used, and this would enable us to obtain data in the marginal area.

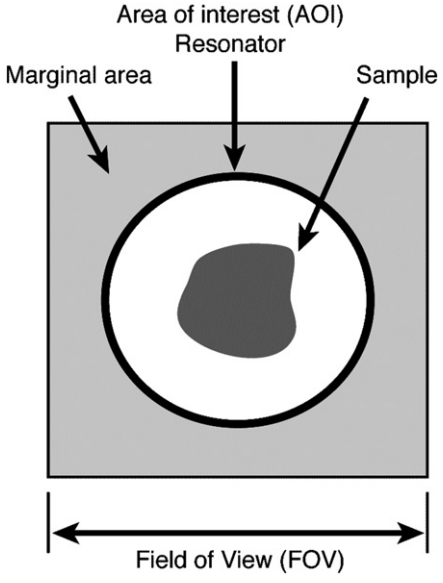


Fig. 2. Marginal area around the area of interest (AOI). The signal in the marginal area is definitely considered noise, since there are no signal sources in the marginal area. The AOI usually corresponds to the physical dimensions of the resonator. By setting the field of view (FOV) greater than the AOI, the marginal area appears. The maximum amplitude of the noise in the marginal area is searched for and used in the evaluation function shown in Fig. 1B.

The following computations are used to measure the noise level in the marginal area:

1. Apply FFT to each projection and the zero-gradient projection.
2. Set the cutoff frequency of the low-pass window function.
3. Perform deconvolution in Eq. (2) for each projection with the window function.
4. Re-grid the data in $k$-space in polar coordinates to Cartesian coordinates.
5. Perform inverse FFT for the data in $k$-space to obtain the ERP image.
6. Measure the noise amplitude in the marginal area, and go back to Step 2.

After detecting the noise level in the marginal area, we multiplied the obtained noise level by 1.5. We then used this value as the threshold to suppress background noise in the AOI. Noise in CW-EPR spectroscopy is considered a random process, so that the probability of the noise amplitude in the AOI that is beyond the maximum noise level in the marginal area is not equal to zero. Thus, we need to add the margin of the noise estimation to achieve robustness for noise suppression. In the AOI, image data that are less than the threshold are set to zero to suppress noise and artifacts.

### 2.5. Implementation of the computation code

We used the DFTR method and searched for the global minimum point of the evaluation function to determine the cutoff frequency of the low-pass window function. We implemented the methods described in this article using Fortran development environment (Absoft Corporation, Pro Fortran for MacOS X v8.2, Rochester Hills, MI) on Mac OS X (Apple Computer, Cupertino, CA). The subroutine FFTCF of the IMSL Fortran Numerical Library (Visual Numerics, Houston, TX) was used for FFT to obtain complex data in $k$-space. In 2D inverse FFT for reconstructing EPR images, we also used the subroutine FFT2B of the IMSL Fortran Numerical Library. To re-grid $k$-space data in polar coordinates to Cartesian coordinates, we used the hybrid two-stage spline-linear interpolation proposed by Matej and Bajla [24]. The size of the matrix was $512 \times 512$ in both the resultant image and $k$-space.

### 2.6. Phantom and EPR imager

We used a home-built 300 MHz CW-EPR imager to test the present method with nine capillary tubes. A resistive Helmholtz coil was used to apply a static magnetic field (10.7 mT for 300 MHz), and three gradient coils were used to apply gradient fields in Cartesian coordinates with three programmable bipolar power supplies (Kikusui Electronics, PBX20-10, Yokohama, Japan). Another Helmholtz coil was used for magnetic field scanning (up to ±5 mT) with a bipolar power supply (PBX20-10). A loop-gap resonator (28 mm in diameter and 30 mm in length) [25,26] was used with a standard reflection-type EPR bridge. Field modulation was applied with a saddle-type coil at 90 kHz, and the first-derivative EPR absorption line was detected with a lock-in amplifier (NF Instruments, LI5640, Yokohama, Japan). Data acquisition and setting of the gradient fields were performed using a LabVIEW-based control program (National Instruments, LabVIEW7, Austin, TX) via an IEEE-488 interface bus. Typical settings of the EPR imager were: applied microwave power 5.6 dBm, field modulation 0.05 mT, scan time 4 s, time constant of the lock-in amplifier 3 ms, field scan width 3 mT, gradient field 100 mT/m, and number of projections 128.

This EPR imager was intended to measure a small rodent such as a mouse. The 300-MHz EPR bridge and electronic circuits in the imager were designed for biomedical applications with a living animal. In our spectrometer setup, the configuration of the RF circuits we used was similar to that of a 1.2-GHz EPR bridge developed at Dartmouth Medical School (Hanover, NH) [27]. Automatic frequency control (AFC) is generally used [28], and automatic tuning control (ATC) and automatic matching control (AMC) can also be used with an electronically tunable resonator [29,30]. The maximum gradient fields were 170 mT/m in the $z$-direction (horizontal in the laboratory and along the static magnetic field) and 120 mT/m in the $x$-direction (vertical in the laboratory). A linear gradient field with an error of less than 5% was obtained within an area that measured 52 mm in the $z$-direction and 30 mm in the $x$-direction.

Nine capillary tubes containing 1,1-diphenyl-2-picrylhydrazyl (DPPH) power were placed in the loop-gap resonator. The inner diameter of the capillary tubes was 1 mm. The tube at the center of the top row contained about 3 mg DPPH powder. The tubes were mechanically supported with a piece of styrene foam, and separated from each other by about 3 mm. The signal intensities of individual capillary tubes were measured with a 300-MHz EPR spectrometer with no gradient magnetic field, and are indicated in Fig. 5A. The conditions of EPR measurements are similar to those for the 2D EPR imaging data acquisition mentioned above.

## 3. Results

For the Hamming window function, we computed the effective width of the PSF as a function of the cutoff frequency, as shown in Fig. 3A. The effective widths were normalized by the FOV. Even if another window function is used, the PSF can be calculated similarly. For a given data set of 128 projections, we estimated the noise level by the method described in Section 2.4. Fig. 3B shows the maximum noise level in the marginal area for the capillary phantom. This can ultimately affect the evaluation function. We used 5-point-average values for the results in Fig. 3B to avoid variance of the noise level. Fig. 3B also shows the smoothed data for the noise level as a function of the cutoff frequency.

The product of two functions, the effective width of the PSF and the maximum noise level, showed a global minimum point, as expected. Fig. 4 shows the product of the data in Figs. 3A and 3B. According to our strategy, the cutoff frequency at the global minimum point in Fig. 4 was determined to be 24. The evaluation function

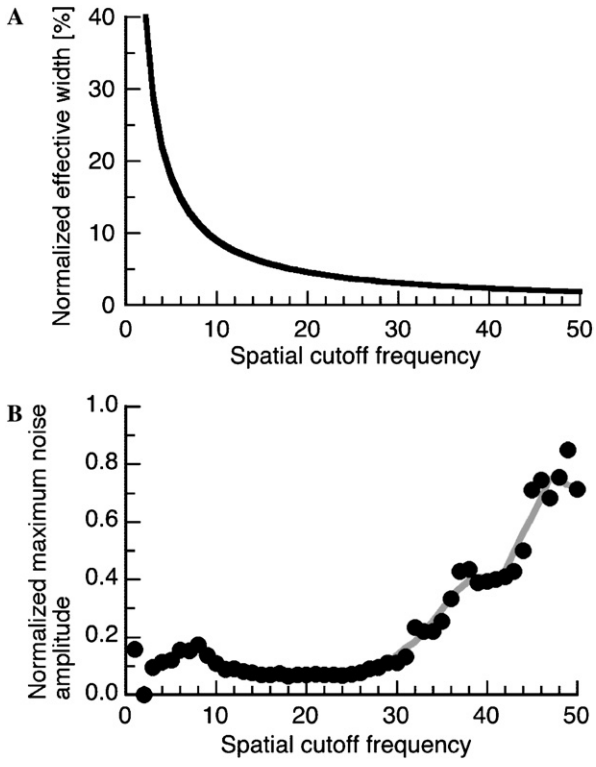


Fig. 3. (A) Calculated normalized effective width of the PSF as a function of the cutoff frequency with the Hamming window function in Eq. (5). (B) Estimated maximum noise level in the marginal area of the resultant images as a function of the cutoff frequency with the Hamming window function in Eq. (5). Closed circles are the results of the maximum noise amplitude in the marginal area, and the gray line shows the 5-point-average values of the data. The maximum noise amplitudes in the marginal area were normalized by the maximum signal in the AOI at each cutoff frequency.

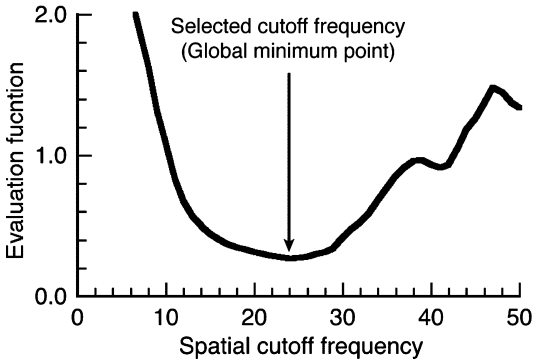


Fig. 4. Product of the effective width of the PSF (Fig. 3A) and the noise level (Fig. 3B) as an evaluation function for determining the cutoff frequency. The global minimum point is 24 for the given projection data set, and this cutoff frequency provides well-compromised results for spatial resolution and noise suppression in the resultant image.

gave large values in both the lower and higher cutoff frequencies.

The signal intensities for the nine capillaries (Fig. 5A) agreed well with the resultant image in Fig. 5B. The threshold was selected to be 10.7% of the maximum signal intensity in Fig. 5B, and the data of signals less than this threshold were replaced by zero to suppress background noise in the image. Fig. 5B is the final image reconstructed from the projection data set. The cutoff frequency was selected to be 24 according to the results of Fig. 4. The cutoff frequency at the global minimum point provided a good compromise in the spatial resolution and noise suppression in the resultant image. To investigate the change in background noise in the resultant images, Fig. 5C shows images with cutoff frequencies from 20 to 28. The threshold was set to zero in these figures. The noise amplitudes in the images were gradually increased when the cutoff frequency increased. Also, fluctuation in the background noise with higher frequency components appeared when a higher cutoff frequency was used.

## 4. Discussion and conclusions

We demonstrated that the product of the effective width of the PSF and the noise level has a global minimum point. This finding is important for finding a good comprise between the two criteria for image quality. The noise amplitude in the resultant image is remarkably increased when the cutoff frequency is increased. When very low frequencies are used for the cutoff frequency, the noise in the image is only slightly increased. This is because frequency components with a very limited bandwidth cannot reconstruct the original signal and make large artifacts in the image. To validate the present method, we compared the results of cutoff frequency selection to those obtained for the same projection data with the previously reported statistical method. This method is based on the calculation of the piecewise variance of the division result of the Fourier amplitude spectra. The details of the statistical method have been described elsewhere [23]. The cutoff frequency was determined to be 24.3 for the same projection data set with the statistical method. This was the mean value of the cutoff frequencies for each projection, and the standard deviation was 1.5. With the present method, the cutoff frequency is selected to be 24, and this agrees well with the result of the statistical method. Without visual inspection, similar results regarding the cutoff frequency were obtained for deconvolution with both methods.

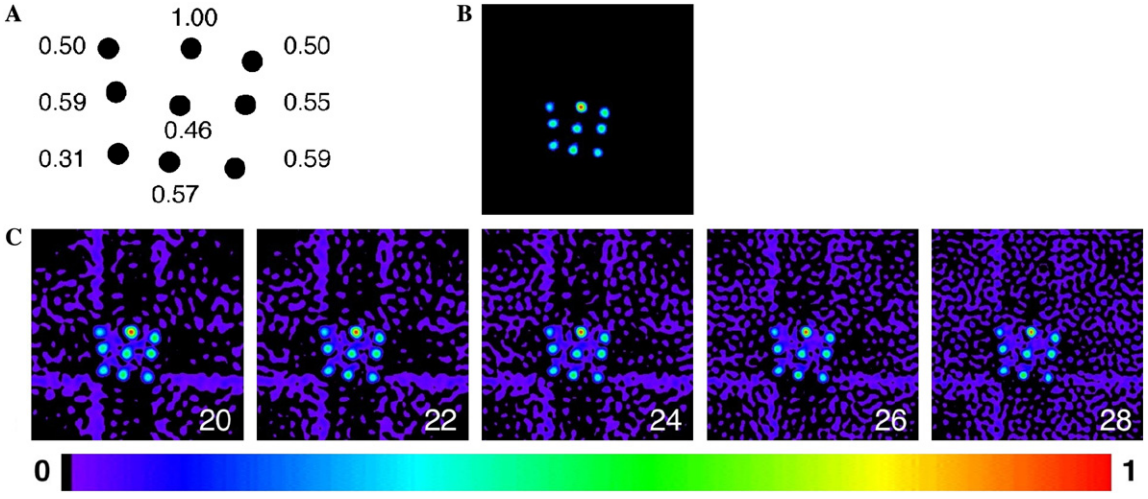


Fig. 5. Resultant EPR images for a phantom that consists of capillary tubes containing 1,1-diphenyl-2-picrylhydrazyl (DPPH) power. (A) Measured signal intensities of the capillary tubes. The signal intensities were normalized by that of the tube at the center of the top row. (B) The resultant image with a spatial cutoff frequency of 24 and a threshold of 10.7% of the maximum signal intensity. (C) Resultant images with a zero-threshold and cutoff frequencies from 20 to 28.

In the resultant image with a Hamming window function with a cutoff frequency of 24, the maximum noise amplitude in the marginal area was 0.071 when the maximum signal in the image was normalized to 1. Furthermore, the standard deviation $\sigma$ of the noise was $1.73 \times 10^{-2}$. Since we used a threshold of 0.107, this corresponds to $6.2\sigma$. The probability that the noise in the AOI beyond the threshold level is very close to zero, when the background noise is expressed by a Gaussian distribution. The threshold we used in the image was appropriate for suppressing the background noise in Fig. 5B. Since the noise is a random process, the mean of the noise in the marginal area should be zero. Thus, we focus on the standard deviation and the maximum noise amplitude. In practice, the threshold has to be greater than the maximum noise amplitude in the image. Otherwise, the background noise could not be suppressed in the resultant image. While the use of the maximum noise amplitude is practical in noise suppression, the use of a statistical quantity such as the standard deviation makes sense for treating the noise as a random process.

A higher threshold could affect the final image. Since the present method gives the threshold based on the noise in the marginal area, overestimation of the threshold is avoided. The evaluation function does not change drastically around the global minimum point, as shown in Fig. 4. This means that cutoff frequency selection is robust for a small variance in the cutoff frequency. This is consistent with the results in Fig. 5. Adaptive control of the cutoff frequency effectively improves the ease of operation in EPR imaging. This makes it possible to obtain a consistent quality of the resultant image, even if multiple users operate the EPR imager and image reconstruction program.

In the present method, automatic selection of the cutoff frequency depends on the evaluation function, as shown in Fig. 1B. However, how does the evaluation function reflect a shift in the field gradient? We tested two experimental conditions for the field gradient, i.e., 100 and 50 mT/m, and the FOV was kept at 30 mm in both measurements. Two capillary tubes containing DPPH powder were measured, and the distance between them was approximately 6 mm. Other experimental parameters were the same as those in Section 2.6. For projections with the higher field gradient (100 mT/m), the cutoff frequency was selected at the spatial frequency of 29, while that with the lower field gradient (50 mT/m) was set at 18. When the lower field gradient was applied, the noise amplitude as a function of the cutoff frequency corresponding to Fig. 3B was shifted to the low frequency band (data not shown). If the pass-band of the window function is very limited, the true profile of unpaired electrons cannot be reconstructed due to a lack of necessary spatial frequency components, and consequently background noise and fluctuation appear. In contrast, if noise in the higher spatial frequencies is in the pass-band of the window function, it significantly increases the noise amplitude everywhere in the resultant image. This is the reason for the shift in the noise characteristics, and the cutoff frequency selection can be adapted to projections with various field gradients as a result.

The spatial resolution is governed by the linewidth of the EPR spectrum and the applied gradient field. Also, it has been reported that deconvolution for projections with a zero-gradient projection can improve the spatial resolution of EPR imaging [20]. In Fig. 3A, the spatial resolution at a cutoff spatial frequency of 24 was 1.14 mm (3.8% of the FOV). This means that the effect of the Hamming window function, instead of the maximum gradient field of the EPR imager, is the main limiting factor of the spatial resolution in our experiments. Good sensitivity of the EPR imager can improve the spatial resolution, since it allows us to use a higher cutoff frequency for the low-pass window function. In preliminary findings, the detectable spin number of our EPR instrument is approximately $1 \times 10^{17}$ spins/0.1 mT with the measurement settings described in Section 2.6. This sensitivity is comparable to a 300-MHz CW-EPR spectrometer reported by a group at National Cancer Institute, National Institutes of Health (Bethesda, MD) [31].

The calculation time for the whole computation is a key practical consideration in EPR image reconstruction. In the present method, reconstruction of a 2D image is needed to estimate the noise level, and this requires a 2D inverse FFT subroutine at each cutoff frequency. If the noise level can be predicted in a resultant image without 2D inverse FFT, the computation time for the present method could be dramatically reduced. In our computation code written in Fortran77, it takes 12 s for 40 calculations to obtain the values of the evaluation function with a personal computer (Apple Computer, PowerMac G5 (dual 2.0-GHz PowerPC 970), Cupertino, CA). This means that the evaluation function can be calculated in only 0.3 s, and the computation time is practically fast enough.

In conclusion, the findings in Figs. 3 and 4 strongly support our hypothesis that the product of the effective width of the PSF and the noise level in the marginal area can be used as an evaluation function for selecting the cutoff frequency of the window function in EPR image reconstruction. The systematically selected cutoff frequency of the window function gives an EPR image with reasonably good resolution and noise suppression. This allows us to improve the reproducibility and ease of operation in EPR imaging instruments. The evaluation function gives a useful guideline for cutoff frequency selection in image reconstruction.

## Acknowledgments

The authors wish to thank Yusuke Murayama for his helpful discussions on noise suppression. This work was supported by a grant from the Japan Society for the Promotion of Science (16560359 to H.H.). Y. Deng was supported by an NIH grant (EB00890).

## References

[1] P. Kuppusamy, J.L. Zweier, Cardiac applications of EPR imaging, NMR Biomed. 17 (2004) 226–239.
[2] Y. Deng, G. He, S. Petryakov, P. Kuppusamy, J.L. Zweier, Fast EPR imaging at 300-MHz using spinning magnetic field gradients, J. Magn. Reson. 168 (2004) 220–227.
[3] A. Blank, C.R. Dunnam, P.P. Borbat, J.H. Freed, Pulsed three-dimensional electron spin resonance microscopy, Appl. Phys. Lett. 85 (2004) 5430–5432.
[4] K. Matsumoto, B. Chandrika, J.A.B. Lohman, J.B. Mitchell, M.C. Krishna, S. Subramanian, Application of continuous-wave EPR spectral-spatial image reconstruction techniques for in vivo oxymetry: comparison of projection reconstruction and constant-time modalities, Magn. Reson. Med. 50 (2003) 865–875.
[5] M. Elas, B.B. Williams, A. Parasca, C. Malier, C.A. Pelizzari, M.A. Lewis, J.N. River, G.S. Karczmar, E.D. Barth, H.J. Halpern, Quantitative tumor oxymetric images from 4D electron paramagnetic resonance imaging (EPRI): methodology and comparison with blood oxygen level-dependent (BOLD) MRI, Magn. Reson. Med. 49 (2003) 682–691.
[6] L.J. Berliner, H. Fujii, Magnetic resonance imaging of biological specimens by electron paramagnetic resonance of nitroxide spin labels, Science 227 (1985) 517–519.
[7] G.R. Eaton, S.S. Eaton, EPR imaging using flip-angle gradients: a new approach to two-dimensional imaging, J. Magn. Reson. 67 (1986) 561–564.
[8] S. Colacicchi, P.L. Indovina, F. Momo, A. Sotgiu, Low-frequency three-dimensional ESR imaging of large samples, J. Phys. E: Sci. Instrum. 21 (1988) 910–913.
[9] K. Ohno, T. Murakami, Microscopic ESR imaging using a microcoil system, J. Magn. Reson. 79 (1988) 343–347.
[10] H.J. Halpern, D.P. Spencer, J. van Polen, M.K. Bowman, A.C. Nelson, E.M. Dowey, B.A. Teicher, Imaging radio frequency electron-spin-resonance spectrometer with high resolution and sensitivity for in vivo measurements, Rev. Sci. Instrum. 60 (1989) 1040–1050.
[11] J.A. Brivati, A.D. Stevens, M.C.R. Symons, A radiofrequency ESR spectrometer for in vivo imaging, J. Magn. Reson. 92 (1991) 480–489.
[12] S. Subramanian, N. Devasahayam, R. Murgesan, K. Yamada, J. Cook, A. Taube, J.B. Mitchell, J.A.B. Lohman, M.C. Krishna, Single-point (constant-time) imaging in radiofrequency Fourier transform electron paramagnetic resonance, Magn. Reson. Med. 48 (2002) 370–379.
[13] G. Placidi, M. Alecci, A. Sotgiu, First imaging results obtained with a multimodal apparatus combining low-field (35.7 mT) MRI and pulsed EPRI, Phys. Med. Biol. 47 (2002) 127–132.
[14] R.W. Quine, G.A. Rinard, S.S. Eaton, G.R. Eaton, A pulsed and continuous wave 250 MHz electron paramagnetic resonance spectrometer, Concepts Magn. Reson. B: Magn. Reson. Eng. 15 (2002) 59–91.
[15] Z.-P. Liang, P.C. Lauterbur, Principles of Magnetic Resonance Imaging: A Signal Processing Perspective, IEEE Press, New Jersey, 2000, Chapter 6.
[16] H. Stark, J.W. Woods, I. Paul, R. Hingorani, Direct Fourier reconstruction in computer tomography, IEEE Trans. Acoust. Speech, Signal Process. 29 (1981) 237–245.
[17] H. Stark, J.W. Woods, I. Paul, R. Hingorani, An investigation of computerized tomography by direct Fourier inversion and optimum interpolation, IEEE Trans. Biomed. Eng. 28 (1981) 496–505.
[18] G. Placidi, M. Alecci, S. Colacicchi, A. Sotgiu, Fourier reconstruction as a valid alternative to filtered back projection in iterative applications: implementation of Fourier spectral spatial EPR imaging, J. Magn. Reson. 134 (1998) 280–286.
[19] A. Feintuch, G. Alexandrowicz, T. Tashma, Y. Boasson, N. Kaplan, Three-dimensional pulsed ESR Fourier imaging, J. Magn. Reson. 142 (2000) 382–385.
[20] F. Momo, S. Colacicchi, A. Sotgiu, Limits of deconvolution in enhancing the resolution in EPR imaging experiments, Meas. Sci. Technol. 4 (1993) 60–64.
[21] Z.-P. Liang, P.C. Lauterbur, Principles of Magnetic Resonance Imaging: A Signal Processing Perspective, IEEE Press, New Jersey, 2000, Chapter 8.
[22] P. Kuppusamy, M. Chzhan, J.L. Zweier, Development and optimization of three-dimensional spatial EPR imaging for biological organs and tissues, J. Magn. Reson. B 106 (1995) 122–130.
[23] Y. Deng, G. He, P. Kuppusamy, J.L. Zweier, Deconvolution algorithm based on automatic cutoff frequency selection for EPR imaging, Magn. Reson. Med. 50 (2003) 444–448.
[24] S. Matej, I. Bajla, A high-speed reconstruction from projections using direct Fourier method with optimized parameters: an experimental analysis, IEEE Trans. Med. Imaging 9 (1990) 421–429.
[25] W.N. Hardy, L.A. Whitehead, Split-ring resonator for use in magnetic resonance from 200 to 2000 MHz, Rev. Sci. Instrum. 52 (1981) 213–216.
[26] W. Froncisz, J.S. Hyde, The loop-gap resonator: a new microwave lumped circuit ESR sample structure, J. Magn. Reson. 47 (1982) 515–521.
[27] T. Walczak, P. Lesniewski, I. Salikhov, A. Sucheta, K. Szybinski, H.M. Swartz, L-band electron paramagnetic resonance spectrometer for use in vivo and in studies of aqueous biological samples, Rev. Sci. Instrum. 76 (2005) 013107.
[28] H. Hirata, Z.-W. Luo, Stability analysis and design of automatic frequency control system for in vivo EPR spectroscopy, Magn. Reson. Med. 46 (2001) 1209–1215, Erratum 49 (2003) 977.
[29] H. Hirata, Y. Yamaguchi, T. Takahashi, Z.-W. Luo, Control characteristics of an automatic matching control system for in vivo EPR spectroscopy, Magn. Reson. Med. 50 (2003) 223–227.
[30] H. Hirata, T. Walczak, H.M. Swartz, Electronically tunable surface-coil-type resonator for L-band EPR spectroscopy, J. Magn. Reson. 142 (2000) 159–167.
[31] J. Koscielniak, N. Devasahayam, M.S. Moni, P. Kuppusamy, K. Yamada, J.B. Mitchell, M.C. Krishna, S. Subramanian, 300 MHz continuous wave electron paramagnetic resonance spectrometer for small animal in vivo imaging, Rev. Sci. Instrum. 71 (2000) 4273–4281.